RESEARCH ARTICLE

In Situ Self-Assembly of Nanoscale Particles into Macroscale Ordered Monolayers with Enhanced Memory Performance

Wang Li[a] #, Ke Sun[b] #, Lisong Yang[c], Xi Mao[a], Shuai Deng[a], Hui Jiang[b], Pan Gu[a], Bowen Cao[b], Wen Li*[b], Mingdong Yi[b], Colin D. Bain*[c], Renhua Deng*[a], and Jintao Zhu*[a]

#These authors contributed equally to this work.

[a] W. Li, X. Mao, S. Deng, P, Gu, R. Deng, J. Zhu
State Key Laboratory of Materials Processing and Die & Mould Technology, Key Laboratory of Materials Chemistry for Energy Conversion and Storage of the Ministry of Education, School of Chemistry and Chemical Engineering.
Huazhong University of Science and Technology
Wuhan 430074, China
E-mail: rhdeng@hust.edu.cn (R. D.); jtzhu@mail.hust.edu.cn (J. Z.);

[b] K. Sun, H. Jiang, B. Cao, W. Li, M. Yi
Key Laboratory for Organic Electronics and Information Displays, Institute of Advanced Materials (IAM)
Nanjing University of Posts & Telecommunications (NUPT)
Nanjing 210023, China
E-mail: iamwli@njupt.edu.cn (W. L.)

[c] L. Yang. C. D. Bain
Department of Chemistry
Durham University
Stockholm Road, Durham DH1 3LE, U.K.
E-mail: c.d.bain@durham.ac.uk (C.D.B.)

Supporting information for this article is given via a link at the end of the document.

Abstract: In situ fabrication of macroscale ordered monolayers of nanoparticles (NPs) on targeted substrates is highly desirable for precision electronic and optical devices, while it remains a great challenge. In this study, we provide a solution to address this challenge by developing a colloidal ink formulation and employing the direct-ink-writing (DIW) technique, where on-demand delivery of ink at a targeted location and directional evaporation with controllable rate are leveraged to precisely guide the deposition of polystyrene-grafted gold NPs (Au@PS NPs) into a macroscale monolayer with an ordered Au NP array embedded in a PS thin film. We proposed a 2D steady-state diffusion-controlled evaporation model, which explains the parameter dependence of the experimental results and gives semiquantitative agreement with the experimental evaporation kinetics. The ordered monolayer is used as both nanocrystal floating gates and the tunneling layer for nonvolatile memory devices. It shows significantly enhanced performance compared with a disordered NP film prepared by spin coating. This approach allows fine control of NP self-assembly to print macroscale ordered monolayers directly onto substrates, which has great promise for application in broad fields, including microelectronic and photoelectronic devices, sensors and functional coatings.

Introduction

Monolayers of functional nanoparticles (NPs)[1], such as Au NPs, have attracted increasing attention in various application fields, including sensing[2], detection[3], and optical and electronic devices[4]. Compared with individual NPs or bulk materials, monolayers of NPs exhibit unique optical, thermal, and electrical properties that arise from synergistic interparticle interactions, such as plasmon coupling and electromagnetic enhancement.[5] In particular, ordered monolayers are of great interest because of their enhanced performance and even new attractive functions.[6] For example, coherent vibrational modes can only appear in highly ordered NP assemblies,[7] and p-type conductivity can be obviously improved via synergistic effects in ordered assemblies.[8] More importantly, uniform and repeatable synergistic properties require overall ordered structures, which are critical for downstream applications in precision devices.[9] For instance, when applied as nanocrystal floating gates for ultrahigh-density data memory devices, the overall order degree has decisive effects on memory performance.[10] However, the fabrication of overall ordered monolayers in macroscale is nontrivial because NPs are notoriously difficult to manipulate due to their complex nanoscale forces with each other.[11] Grafting NPs with soft ligands, such as polymers, is an effective way to manipulate their nanoscale forces.[12] Polymer ligands can prevent NPs from disordered aggregation, allow fine-tuning of the self-assembled structures and interparticle distances, and provide stimulus responses and other functions.[12b,12c,13]

Bottom-up interfacial self-assembly of colloidal particles on 2D surfaces or interfaces has been widely applied to construct monolayers, where self-assembly is driven by solvent evaporation, changes in particle solubility, or external fields.[14] In this respect, many efforts have been made towards the gas–liquid or liquid–liquid interfacial self-assembly of NPs, which leave behind monolayers on the surface of liquid supports.[15] The effects of various parameters (such as ligand chemicals or length or grafting density,[1e, 11, 16] core size[16b], solvent,[17] and temperature[18]) on the structures of monolayers have been comprehensively studied.

Macroscale ordered monolayers of NPs are accessible on liquid supports through careful handling in some cases, followed by transfer printing to targeted solid substrates for applications.[19] In contrast, transfer process is not needed through the *in situ* self-assembly of NPs on targeted substrates, which can avoid cracking and wrinkling of these ultrathin monolayers during the cutting and transfer process. The common techniques for deposition of NPs on substrates include spin coating, slot-die coating, drop casting, Langmuir-Blodgett technology, and printing.[15a,15c,20] Because of the presence of a fixed solid substrate, the self-assembly of NPs into macroscale ordered monolayers becomes more difficult,[21] and a well-known adverse factor is the so-called coffee-ring effect.[22] Convective assembly has been proven to be effective for the generation of ordered monolayers of micron and sub-micron colloidal particles,[20d, 20g] yet the preparation of ordered monolayers of NPs is much more difficult because the evaporation and convections usually occur at a much larger volume than NP size.[20f] Micropattern-assisted confinement enables convective assembly of NPs into monolayers inlaid in pores or channels.[20e, 20f, 23] However, it remains a great challenge to prepare ordered NP monolayers in the macroscale. Nevertheless, impressive advances in terms of the effects of various parameters on NP self-assembly or aggregation would provide important guidance in the preparation of macroscale ordered NP monolayers on solid substrates.

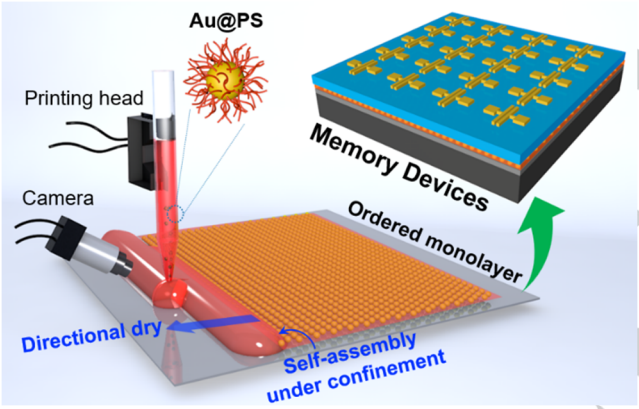

Scheme 1. Schematic illustration of an ordered monolayer printed by DIW and its application in memory devices.

In this work, a solution is provided to address this challenge with a 2D steady-state diffusion-controlled evaporation-driven self-assembly strategy by employing direct-ink-writing (DIW) technology (**Scheme 1**). We leverage the advantages of DIW, such as digital localized continuous delivery and directional evaporation, to precisely guide the self-assembly of polystyrene-grafted Au NPs (Au@PS NPs) during the printing process. By cooperative control of printing parameters (including the distance between the centres of two adjacent printed lines and drying temperature) and ink formulation (including concentration, solvent, and length of ligand), we confirm that the synergistic effect between on-demand NP delivery and directional evaporation-induced assembly under confinement is critical for forming ordered monolayers. We propose a model in which the evaporation of the ink in the DIW process approximates the 2D steady-state, diffusion-controlled evaporation of a liquid ridge, which explains the parameter dependence of the experimental results. The calculation gives semiquantitative agreement with the experimental evaporation rates, and simulations reproduce the time variation of the width of the wetted film. In addition, DIW has other inherent advantages, such as the efficient use of materials, scalability, and reliability. Benefiting from the ordered structure, the monolayer of Au@PS NPs shows good performance as nanocrystal floating gates, as well as a charge trapping layer and tunneling layer for nonvolatile memory devices.

Results and Discussion

(1) Ink Formulation and Morphology of Macroscale Ordered Monolayers.

Uniform Au@PS NPs with an Au core (diameter, Φ = 14.49 ± 0.99 nm) and PS brushes (number-average molecular weight, 22 kg/mol, i.e., PS_{22k}) were synthesized (see Figure S1a in the Supporting Information). This classical Au@PS NP system is chosen because: 1) it is one of the most concerning and well-built systems;[16b, 23, 24] 2) from the application perspective of this study, Au NPs are excellent nanocrystal floating gates for hole trapping because of their excellent chemical stability and high work function;[3a, 6b] at the same time, PS can serve as the tunneling layer and electron-trapping layer because of its nice insulation and long charge relaxation time.[3a, 25] A high boiling (*b.p.* = 202 °C) and super-wettability solvent (contact angle: ~ 0°, Video S1), N-methylpyrrolidone (NMP), was selected as the solvent for Au@PS NPs to form colloidal inks. A continuous fluid of the ink was delivered onto the target substrate (Si wafer with a 300 nm SiO_2 layer) from the nozzle (inner diameter: *ca*. 50 μm) along an 'S' route, resulting in a macroscopic uniform film with an area of 1 cm^2 after drying (**Figure 1**a). The high homogeneity of the overall film was confirmed by SEM under low magnification, where a large region of 300 μm × 300 μm is shown (Figure 1b). A high-magnification SEM image indicates that Au@PS NPs self-assembled into an ordered hexagonal structure with a period distance of 33.95 ± 2.17 nm (Figure 1c). The fast Fourier transform (FFT) image of the SEM image confirms the high degree of order of the NP array (the inset of Figure 1c). The roughness and thickness of the film were studied by AFM. A low magnification AFM image shows a root mean square roughness (*Rq*) as low as 0.71 nm for a relatively large area up to 17 μm × 17 μm (Figure 1d). Its thickness was measured as *ca*. 22 nm according to the cross-sectional height profile (Figure 1e and 1f), indicating that it is a monolayer.

(2) Effect of Experimental Parameters on the Morphology of Deposits.

The formation of such ordered monolayers can be explained by the convective assembly of NPs under confinement.[20c, 20f] In our study, due to the super-wettability of the solvent (NMP) with the targeted substrate, the thin liquid film of spread ink provides confinement for the self-assembly of Au@PS NPs. In addition, the DIW process is a kind of "2D additive manufacturing", which enables the formation of macroscale monolayers via precise cont-

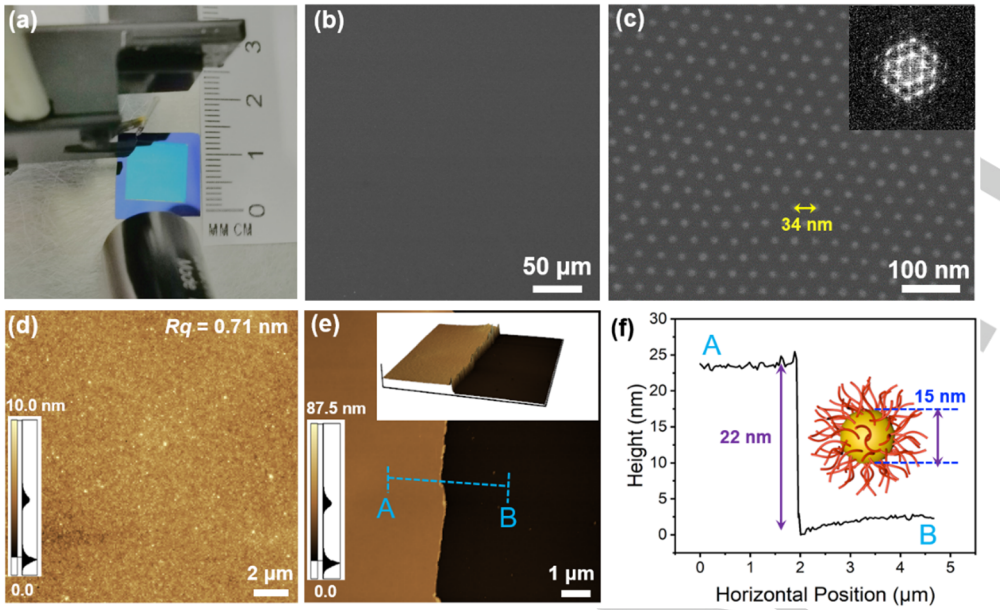

Figure 1. (a) A photograph of a 1 cm × 1 cm monolayer of printed Au@PS NPs; (b) a low magnification and (c) a high magnification SEM images of the monolayer, the inset of (c) is an FFT image; (d-f) AFM images showing the roughness (*Rq*) and height profile of the monolayer, inset of (e) is the 3D image.

rol of the printing parameters and ink formulation. A suitable numerical density on area (ρ_{NA}) of NPs is required to form a monolayer, $\rho_{NA} = n_{NP}/S$. In this study, the total area $S = L_x \times L_x$ (e.g., 1 cm × 1 cm), where L_x and L_y are the width of the deposit along the x- and y-direction, respectively. Therefore, ρ_{NA} equals n_{NP} (number of NPs) in number. The delivered actual number of NPs is calculated by **Equation 1:**

$$n_{NP} = CV_{ink} = CQt = \frac{CQ\left(\frac{L_y}{d}+1\right)L_x}{u} \qquad \textbf{(Eq. 1)}$$

where C is the number of NPs per unit volume in the ink, V_{ink} is the total volume of ink printed, and Q is the average volume of ink printed per unit time (Q depends on jetting voltage and nozzle movement speed, u). The printing time (t) equals the total length of the printed path divided by the nozzle movement speed (u), where the total length of the printed path equals the length of each printing line (L_x) multiplied by the line numbers ($L_y/d + 1$), and d is the distance between the centres of two adjacent printed lines. Under defined u and Q, the delivered n_{NP} can be tuned by varying d or C to meet the requirement for a monolayer ($n_{NP} \approx n_{ML}$).

DIW allows fine control over d, a core parameter determining the morphology of deposits. The printed single line width, $2R$, was *ca.* 240 μm when u = 7.5 mm s^{-1} (Figure S2), and the d value was set lower than that ($d < 2R$) for printing to obtain an integrated film. For a particular value of C, we found that a uniform monolayer of NPs can be obtained when d = 75 μm (Figure S3c). When the d value was decreased to 62.5 μm, partial overlap of NPs (double layer) was observed (Figure S3b), indicating excess NPs ($n_{NP} > n_{ML}$). In contrast, when the d value increased to 87.5 μm, a monolayer with a few blank regions was observed (Figure S3d), indicating that there were too few NPs to cover the whole printed region ($n_{NP} < n_{ML}$). Similar results were obtained by varying C (is proportional to mass concentration) instead of d (Figure S4).

On the other hand, the self-assembly of NPs is driven by evaporation. Therefore, the evaporation speed (E_s), which can be tuned by controlling the substrate temperature (T), plays a key role in determining the morphology of deposits. Via a series of contrast experiments (Figure S5), we found that a moderate temperature (T = 48 °C) provided the correct balance between NP delivery, diffusion and evaporation-induced self-assembly in the current system (Figure 1). If the solvent evaporates too fast, it might induce premature drying of the former printing line and thereby induce overlay of NPs. In addition, faster evaporation means a shorter time for NP diffusion and self-assembly, which may also result in disordered structures. In addition, perturbation from the printhead is adverse to the self-assembly of NPs when the three-phase contact line (TPCL) is close to the printhead. Therefore, a visibly nonuniform deposit was generated when the temperature was increased to 55 °C (Figure S5a). In contrast, if the solvent evaporates too slowly, there is excessive ink on the substrate, which can flow under capillary action to the final printed line, leaving a larger ridge of NPs after drying (Figure S5f). The DIW system (**Figure 2**a) allows visualization of the width (y-direction) of the wetted ridge, $w(t)$, during printing (Video S2 and Video S3). The dynamic maximum width at the middle of the liquid ridge, $w(t)$, as a function of time is shown in Figure 2b. It is measured manually from snapshots of Video S2 and Video S3. We observed that the width increases with time until it reaches nearly a constant value, w_s (Figure 2b). Schemes and representative snapshots are shown in Figure 2c and 2d. The constant width indicates a steady-state in which the evaporative flux is balanced by a source of fluid injected. Under a higher (or lower) temperature, the wetted ridge reaches w_s in a shorter (or longer) time (Figure 2b) with a narrower (or wider) width (Figure 2e). At the end of printing (t > 225 s), $w(t)$ decreases rapidly to zero (not shown in Figure 2b) because no ink was injected.

In addition, the role of ink formulation (including concentration, solvent properties and ligand length) on the morphology of deposits was studied. We have shown that the concentration that affects n_{NP} has a significant impact on the morphology of deposits (see Figure S4). On the other hand, solvent properties (Table S1) have major impacts on the morpho-

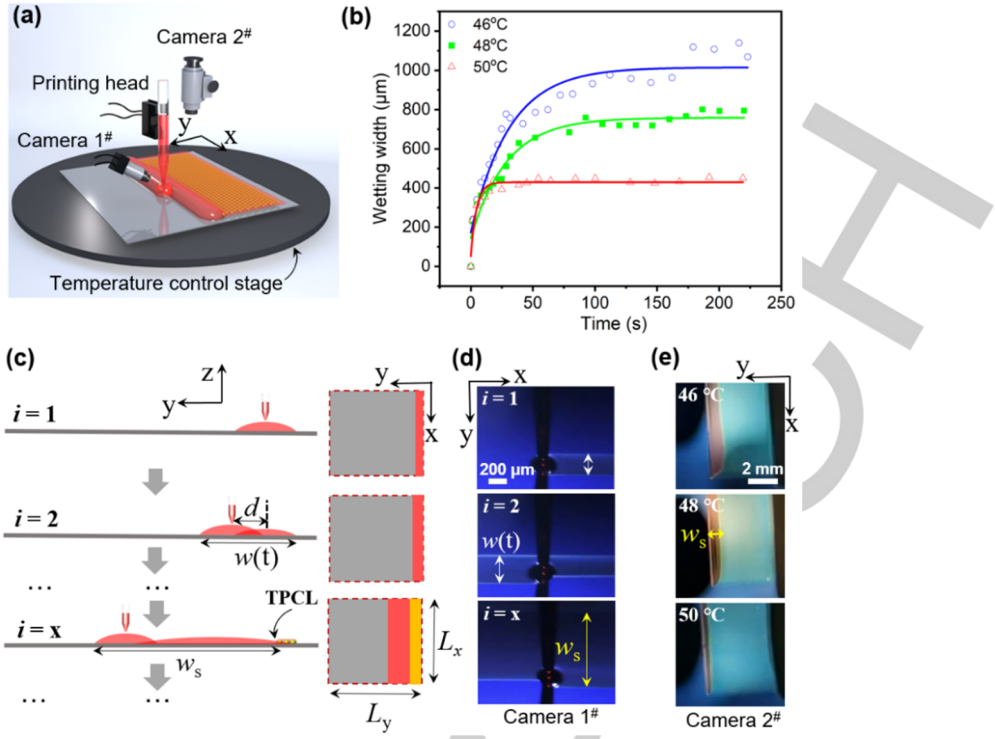

Figure 2. (a) Illustration of the DIW printer with an additional heating stage. (b) Width (y-direction) of wetted ridges as a function of time (t) showing evaporation kinetics during DIW at different temperatures. (c) Illustration of the evolution of the wetted ridge (red) and (d) corresponding photographs captured from camera 1#. (e) Captured photographs from camera 2# showing wetted ridges at their steady-states under different temperatures.

logy of deposits, because the solubility of solvent determines the colloidal stability of NPs,[26] and the wettability of solvent affects the self-assembly of NPs.[20g] We show that the solvent for the preparation of monolayers can be extended to other good solvents (for PS ligand) that also have nice wettability (with receding contact angle θ_c < 15°), such as cyclohexanone and mesitylene (Figure S6a and S6b). We note that the period distance of NPs is independent of solvent. In contrast, in the case of good solvents but with poorer wettability (θ_c > 20°), such as diethylene glycol monoethyl ether acetate (DGMEA), a non-uniform deposit with partial multi-layers and blank regions was observed (Figure S6c). This is mainly because the confinement is not strong enough for convective assembly.[20g] In another control experiment, when a poor solvent (ethylene glycol, EG) was mixed with NMP, aggregations of NPs were observed in the ink or during the printing-drying process depending on the volume ratio of EG/NMP and ink concentration (Figure S7). In addition, the effect of ligand length on the morphology of deposits was also studied. We show that the period distance can be adjusted by varying the ligand length (Figure S8). However, deposits of NPs with short ligands are not uniform monolayers (Figure S8a, S8d). This is possibly because NPs with shorter ligands assemble at a stage where the liquid film is relatively thick (the confinement is not enough).[27] These results indicate that ligands play a key role in determining the morphology of deposits.

(3) Modelling the Printing and Drying Process.

Reaching a steady-state is central to the ability of the DIW method to produce uniform deposits of NPs over "large areas".[20c] Under optimal deposition conditions, the DIW process can be approximated by a 2D steady-state in which a long, thin ridge of liquid receives a constant source of liquid at the leading edge (with flow rate Q) and evaporates at the same rate at the trailing edge. The liquid ridge is stationary in a frame of reference in which the substrate moves at a constant speed in the negative y-direction with magnitude $u_y \approx ud/L_x$ (see **Figure 3**a). To approximate the liquid ridge as long and thin, we require $L_x/w_s >> 1$. Edge effects are limited to a region ~ w_s from the end of each printed line (Figure 2d). For the liquid evaporating at the TPCL to 'see' only an average input flux, rather than responding to the instantaneous position of the nozzle, we seek $w_s/d >> 1$. This inequality ensures that the nozzle only makes a small perturbation to the width of the wetted ridge and that the evaporation time, $(W_s/d)\times(L_x/u)$, is long compared to the time taken to write each line, L_x/u. To prevent the trailing edge from roughening due to capillary instabilities, we require that evaporative flows dominate over capillary flows: $\Omega = \varepsilon^3/\mathrm{Ca} << 1$, where ε is the aspect ratio (height/width) of the ridge and the capillary number $\mathrm{Ca} = u_y\eta/\gamma$, where η is the viscosity and γ is the surface tension of the solvent.[28] Under the experimental conditions, Ca is O (10^{-6}), we thus require that $\varepsilon < 10^{-2}$, i.e., the liquid ridge is very flat. If $\Omega << 1$, the capillary flows that lead to the well-known coffee-ring effect are also suppressed. To obtain such a low value of ε, the solvent must completely wet the substrate. Furthermore, since the height of the ridge is on the order of Q/ud, the aspect ratio $\varepsilon \sim Q/udw_s$. Finally, the evaporation at the TPCL needs to be slow enough that the NPs form an ordered lattice rather than an amorphous film, a condition that is currently empirically determined rather than predicted. Typical values of the experimental parameters that yield a uniform monolayer of NPs satisfy the steady-state conditions above.

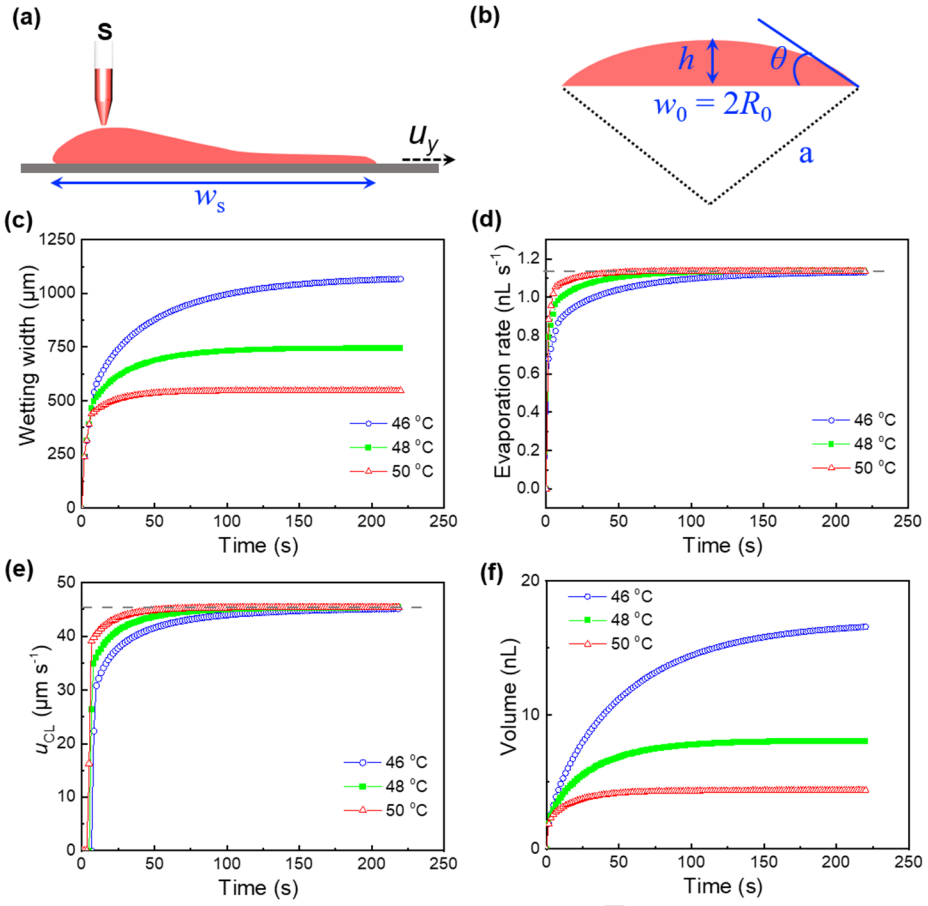

Figure 3. (a) Illustration of steady-state in the 2D model in a frame of reference moving at speed $-u_y$. (b) Definition of parameters for a single printed line. (c) Wetting width, (d) evaporation rate, (e) TPCL movement speed, and (f) volume of the wetted ridge as a function of time for NMP at various temperatures. The dashed lines in (d) and (e) are an average flow rate of 1.13 nL s^{-1} and printer speed in the y-direction of 46 μm s^{-1}.

To make the model more quantitative, we note that the Peclet number Pe is O (10^{-3}), where Pe = $u_y w_s/D_v$ and D_v is the diffusion coefficient of the solvent vapour in air. We can thus solve the steady-state problem of the evaporation of a 2D liquid ridge on a moving substrate under the assumption that evaporation is diffusion controlled. There is no steady-state solution to the 2D-diffusion equation in a semi-infinite space, so we have to introduce an upper length scale at which diffusion becomes three-dimensional. The natural length scale to choose is $L \approx L_x$ (=L_y). With this cut-off, we can evaluate the steady-state evaporation rate E_s (m^3 s^{-1}).

$$E_s = -f(\theta, L/w_s)\frac{\pi M_w D_v}{\rho}\frac{p}{RT}\left[ln\left(\frac{L}{w_s}\right)\right]^{-1} L \qquad \textbf{(Eq. 2)}$$

where D_V is 9 × 10^{-6} m^2 s^{-1}, ρ is the density of NMP (~ 1 kg m^{-3}), p is the saturated vapour pressure (0.18, 0.21 and 0.235 kPa for T = 46, 48 and 50 °C, Figure S9), M_W is the molar weight (99 g mol^{-1}) and R is the gas constant. The numerical pre-factor $f(\theta, L/w_s)$ is of the order of unity and is exactly equal to 1 for a hemicylindrical ridge (i.e., a contact angle of 90°) and a zero-concentration boundary condition at a distance $L/2$ from the centre of the line. Yarin et al. and Schofield et al. have provided solutions for the evaporative flux for variable θ for specific boundary conditions.[29] Eq. 2 is instructive because it shows that the evaporation rate is only weakly (logarithmically) dependent on the choice of the upper cut off, L, and on the width of the ridge, w_s. Taking w_s = 740 μm for T = 48 °C according to the experiment and $f(\theta, L/w_s)$ = 1, we find E_s = 0.85 nL s^{-1}, which is close to, but slightly lower than, the average flow rate of 1.13 nL/s from the experiment. Typically, there are two reasons why the 2D diffusion-controlled steady-state model underestimates the evaporation rate. The first is that diffusion into the 'third' (x) dimension is not negligible, especially near the end of the printed lines. Indeed, we observe the effect of increased evaporation near the ends in a reduction in w_s, which causes the TPCL to be curved (Figure 2d). The second is that we have neglected convection in the model. While a calculation of Pe based on u_y implies that we can neglect convection, the same is not true for the motion of the printhead itself. The airflow caused by the printhead scanning back and forth across the sample will enhance the mass transport of the vapour by convection and hence increase the evaporation rate. Furthermore, NMP vapour is denser than air, which may cause density-driven convection in the vapour. Nevertheless, the reasonably close agreement between the 2D model and the experiment suggests that conceptualizing the DIW process as the evaporation of a 2D ridge is justified.

To simulate the data in Figure 2b, we consider DIW printing as two separate processes: printing a line with rapid coalescence of each line with the wetted film and slow evaporation of the wetted film. We use Eq. 2 to calculate the width-dependent evaporation rate with a constant correction factor, α, and replace

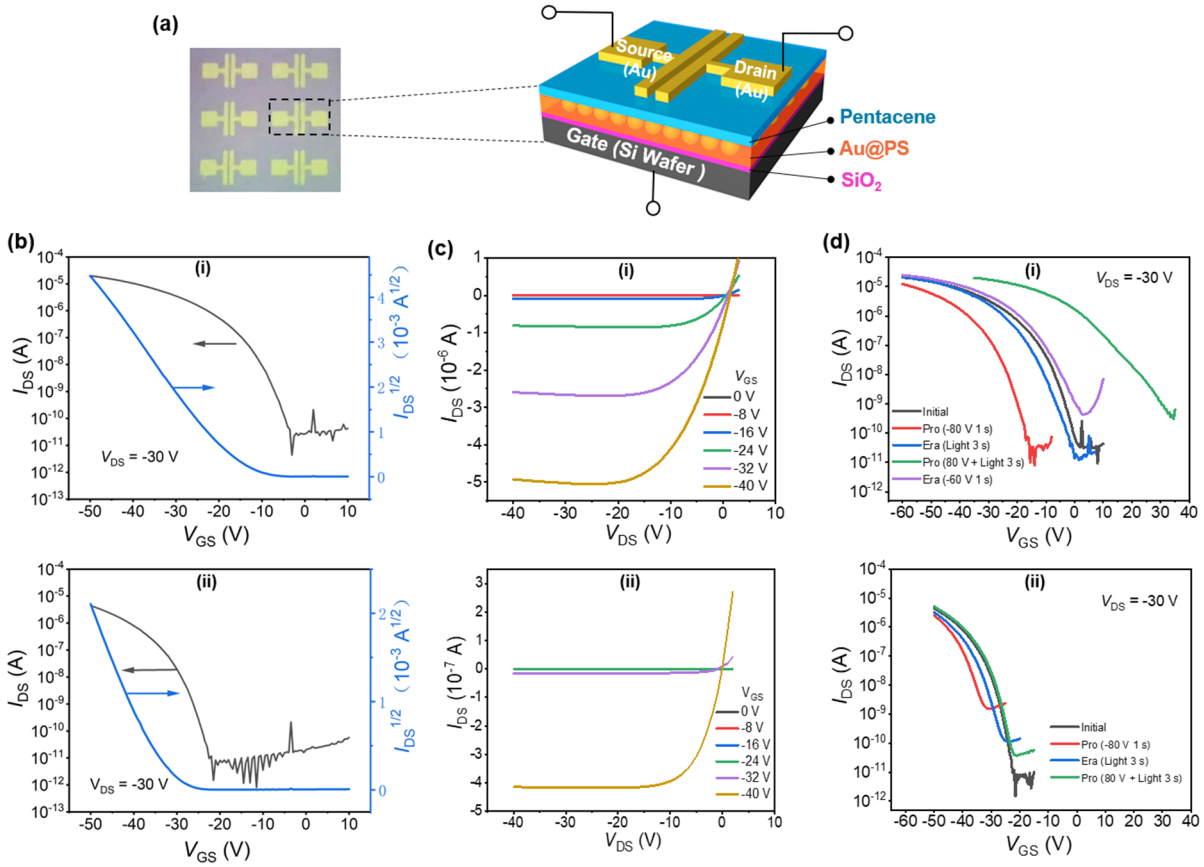

Figure 4. (a) Photograph of an NFGM array with a bottom-gate/top-contact architecture and a schematic illustration. (b) Transfer, (c) output characteristics and (d) programming (Pro)/erasing (Era) threshold voltage transfer curves of an NFGM with (i) the ordered monolayer functional layer and (ii) the disordered functional layer (control).

w_s with $w(t)$. We chose α in the simulation to reproduce the steady-state experimental condition, i.e., a maximum wetting width of 740 μm at T = 48 °C and obtained α = 1.34. This parameter, α, is then used to simulate cases for T = 46 and 50 °C. Figure 3c shows that the temporal evolution of the wetting width and its maximum at the steady-state of the liquid ridge are qualitatively in agreement with the experimental results (see Figure 2b). The simulation also allows us to estimate the dynamic evaporation rate and volume of the wetted ridge, as well as the TPCL movement speed (Figure 3d-f). From the volume of the ink in the wetted film and its width, we can also estimate the steady-state value of $\varepsilon = 2 \times 10^{-3}$, treating the liquid line as a cylindrical cap. This value of ε satisfies the inequality $\Omega << 1$.

The theoretical model and simulations allow us to predict w_s from known properties of the solvent and to select experimental parameters that will meet the requirements set out in the model for 2D steady-state evaporation and hence that will yield a uniform monolayer of NPs.

(4) Performance of Au@PS NP Monolayers for Nanocrystal Floating Gate Memories (NFGMs).

Due to the electron-trapping ability of dielectric PS and the excellent hole-trapping ability of Au NPs, monolayers with Au NP arrays embedded in a PS thin film show attractive application in nonvolatile NFGMs. A highly flat and ordered monolayer was applied as a functional layer for bottom-gate/top-contact NFGMs (**Figure 4**a), where the 300 nm thick silica layer on the top of substrate was applied as the blocking layer and pentacene was applied as the channel. The representative transfer and output curves (Figure 4b$_i$ and 4c$_i$) revealed that the device demonstrates typical p-type field-effect behavior. The hole mobility (μ) and ON/OFF current ratio are calculated to be 0.22 cm^2 V^{-1} s^{-1} and 1.18 × 10^6, respectively. In a control experiment, the memory performance of a NFGM with a disordered functional layer prepared by spin coating (Figure S10) was compared (Figure 4b$_{ii}$ and 4c$_{ii}$). The calculated hole mobility (μ) of the device with the disordered functional layer is only 0.09 cm^2 V^{-1} s^{-1}. This indicates that the smooth PS/pentacene interface of the ordered monolayer facilitates hole transport in the conductive channel.

Reversible threshold voltage (V_{TH}) shifts were performed to evaluate the charge trapping capability of the NFGMs with the ordered functional layer. The memory window is defined as the difference between V_{TH} of the programmed and erased states. As shown in Figure 4d$_i$, after applying a gate voltage of -80 V for 1 s, the transfer curve shifted from the initial position towards the negative voltage direction, indicating that hole trapping occurs in the device. Subsequently, the transfer curve shifted back to the initial position when the device was illuminated with light for 3 s, which resulted in a memory window of 16.1 V for hole trapping. Similarly, a memory window of 35.2 V for electron trapping was achieved by applying a voltage of 80 V with light illumination for 3

s and a subsequent gate voltage of -60 V for 1 s. Again, the reversible threshold voltage shifts benefit from the smooth PS/pentacene interface. The ambipolar trapping of both holes and electrons demonstrates the high charge-storage capacity of the NFGMs with the ordered functional layer. In contrast, the transfer curve slightly shifted from the initial position towards the negative voltage direction after applying a gate voltage of -80 V for 1 s, indicating poor hole trapping ability of the disordered functional layer (Figure 4b_{ii}). In addition, the transfer curve could not shift back to the initial position when the device was illuminated with light for 3 s, indicating that holes could not be effectively transported out. This is because of the presence of many traps at the pentacene/PS interface, coming from the rough surface of the disordered functional layer. For the same reason, nearly no positive shift was obtained by applying a voltage of 80 V with light illumination for 3 s. Therefore, the disordered functional layer only exhibits unipolar trapping of holes with a narrow memory window. On the other hand, the device with the ordered functional layer exhibits high endurance with an I_{ON}/I_{OFF} of more than 10^3 after 100 programming/erasing cycles (Figure S11), while programming/erasing cycles are not achievable from the NFGM with the disordered functional layer.

As summarized in **Table 1**, all key structure/performance parameters of the ordered monolayer prepared by DIW and the corresponding NFGM are significantly superior to those of the disordered film prepared by spin coating. In addition, the usage of NPs by DIW (*ca.* 0.25 μL) is much lower than that by spin coating (> 5.0 μL). These results suggest that the ordered monolayer prepared by DIW is attractive for high-performance nonvolatile NFGMs.

Table 1. Summary of key parameters of the ordered monolayer by DIW and the disordered film by spin coating and corresponding NFGMs.

Parameters	DIW	Spin coating (control)
Morphology	Ordered monolayer	Disordered film
ΔV_{TH} (V)	51.3	8.22
$\Delta V_{TH\text{-}E}$ (V)	35.2	2.46
$\Delta V_{TH\text{-}H}$ (V)	16.1	5.76
μ ($cm^2\ V^{-1}\ s^{-1}$)	0.22	0.09
I_{ON}/I_{OFF}	1.18×10^6	8.0×10^5
NP usage (mg)	ca. 0.01	> 0.2

Conclusion

In summary, we have developed a printing method to address the challenge of the *in situ* fabrication of macroscale ordered monolayers of NPs at targeted locations on substrates. We show that the synergistic effect between NP delivery and evaporation-induced self-assembly under confinement is critical in the formation of ordered monolayers by combining experiments and simulations. We propose a model in which the DIW process proceeds via 2D steady-state, diffusion-controlled evaporation, which explains the parameter dependence of the experimental results. The ordered monolayer of Au@PS NPs exhibits good performance as nanofloating gates, a charge trapping layer and a tunneling layer for nonvolatile memory. This approach allows controllable self-assembly of NPs into ordered monolayers at the macroscale (wafer scale is accessible by printing arrays if required) directly onto patterned substrates with minimum NP usage, which represents an important step toward practical applications in broad fields, including microelectronics, photoelectronic devices, and sensors.

Acknowledgements

We gratefully acknowledge the financial support from the National Natural Science Foundation of China (51933005, 62174089, 61775100 and 61805203). We also acknowledge the HUST Analytical and Testing Center for providing characterization services.

Keywords: gold nanoparticles • monolayers • self-assembly • direct-ink-writing • nanocrystal floating gate

[1] a) C. Yi, Y. Yang, B. Liu, J. He, Z. Nie, *Chem. Soc. Rev.* **2020**, *49*, 465; b) M. S. Lee, D. W. Yee, M. Ye, R. J. Macfarlane, *J. Am. Chem. Soc.* **2022**, *144*, 3330-3346; c) L. Song, Y. Huang, Z. Nie, T. Chen, *Nanoscale* **2020**, *12*, 7433-7460; d) Q. Shi, W. Cheng, *Adv. Funct. Mater.* **2020**, *30*, 1902301; e) W. Mai, Y. Zuo, X. Zhang, K. Leng, R. Liu, L. Chen, X. Lin, Y. Lin, R. Fu, D. Wu, *Chem. Commun.* **2019**, *55*, 10241-10244; f) Zhou, Y.; Han, S. T.; Xu, Z. X.; Roy, V., Controlled ambipolar charge transport through a self-assembled gold nanoparticle monolayer. *Adv. Mater.* **2012**, *24*, 1247-1251.

[2] a) M. A. Boles, M. Engel, D. V. Talapin, *Chem. Rev.* **2016,** *116*, 11220-11289; b) H. Schlicke, S. Kunze, M. Rebber, N. Schulz, S. Riekeberg, H. K. Trieu, T. Vossmeyer, *Adv. Funct. Mater.* **2020,** *30*, 2003381.

[3] a) M. Kang, K. J. Baeg, D. Khim, Y. Y. Noh, D. Y. Kim, *Adv. Funct. Mater.* **2013,** *23*, 3503-3512; b) D. Dong, R. Fu, Q. Shi, W. Cheng, *Nat. Protoc.* **2019,** *14*, 2691-2706.

[4] a) N.-N. Zhang, X. Shen, K. Liu, Z. Nie, E. Kumacheva, *Acc. Chem. Res.* **2022**, *55*, 1503-1513; b) Y. Wang, G. J. Desroches, R. J. Macfarlane, *Nanoscale* **2021**, *13*, 426-443.

[5] a) S. Si, W. Liang, Y. Sun, J. Huang, W. Ma, Z. Liang, Q. Bao, L. Jiang, *Adv. Funct. Mater.* **2016,** *26*, 8137-8145; b) X. Lu, Y. Huang, B. Liu, L. Zhang, L. Song, J. Zhang, A. Zhang, T. Chen, *Chem. Mater.* **2018,** *30*, 1989-1997; c) W. Cheng, N. Park, M. T. Walter, M. R. Hartman, D. Luo, *Nat. Nanotechnol.* **2008,** *3*, 682-690; d) V. Santhanam, R. P. Andres, *Nano Lett.* **2004,** *4*, 41-44.

[6] a) Y. Chen, Y. J. Yoon, X. Pang, Y. He, J. Jung, C. Feng, G. Zhang, Z. Lin, *Small* **2016**, *12*, 6714-6723; b) S. T. Han, Y. Zhou, Z. X. Xu, L. B. Huang, X. B. Yang, V. Roy, *Adv. Mater.* **2012,** *24*, 3556-3561; c) G. Muralidharan, N. Bhat, V. Santhanam, *Nanoscale* **2011**, *3*, 4575-4579; d) S. T. Han, Y. Zhou, C. Wang, L. He, W. Zhang, V. Roy, *Adv. Mater.* **2013,** *25*, 872-877; e) Y. Zhou, S.-T. Han, Z.-X. Xu, V. Roy, *Nanoscale* **2013**, *5*, 1972-1979; f) H. Lin, L. Song, Y. Huang, Q. Cheng, Y. Yang, Z. Guo, F. Su, T. Chen, *ACS Appl. Mater. Interfaces* **2020,** *12*, 11296-11304.

[7] a) B. Gao, M. J. Rozin, A. R. Tao, *Nanoscale* **2013**, *5*, 5677-5691; b) A. Courty, A. Mermet, P. Albouy, E. Duval, M. Pileni, *Nat. Mater* **2005,** *4*, 395-398.

[8] J. J. Urban, D. V. Talapin, E. V. Shevchenko, C. R. Kagan, C. B. Murray, *Nat. Mater.* **2007**, *6*, 115-121.

[9] a) J. Zhang, P. J. Santos, P. A. Gabrys, S. Lee, C. Liu, R. J. Macfarlane, *J. Am. Chem. Soc.* **2016**, *138*, 16228-16231; b) C. A. Bohannon, A. J. Chancellor, M. T. Kelly, T. T. Le, L. Zhu, C. Y. Li, B. Zhao, *J. Am. Chem. Soc.* **2021**, *143*, 16919-16924; c) J. Choi, H. Dong, K. Matyjaszewski, M. R. Bockstaller, *J. Am. Chem. Soc.* **2010**, *132*, 12537-12539; d) A. Abdilla, N. D. Dolinski, P. De Roos, J. M. Ren, E. Van Der Woude, S. E. Seo, M. S. Zayas, J. Lawrence, J. Read de Alaniz, C. J. Hawker, *J. Am. Chem.*

Soc. **2020**, *142*, 1667-1672; e) A. M. Hung, C. M. Micheel, L. D. Bozano, L. W. Osterbur, G. M. Wallraff, J. N. Cha, *Nat. Nanotechnol.* **2010**, *5*, 121-126.

[10] a) K. Wang, H. Ling, Y. Bao, M. Yang, Y. Yang, M. Hussain, H. Wang, L. Zhang, L. Xie, M. Yi, *Adv. Mater.* **2018**, *30*, 1800595; b) T. Zhang, D. Guerin, F. Alibart, D. Troadec, D. Hourlier, G. Patriarche, A. Yassin, M. Oçafrain, P. Blanchard, J. Roncali, *Nanoscale Adv*. **2019**, *1*, 2718-2726.

[11] K. J. Si, Y. Chen, Q. Shi, W. Cheng, *Adv. Sci.* **2018**, *5*, 1700179.

[12] a) J. Pyun, K. Matyjaszewski, T. Kowalewski, D. Savin, G. Patterson, G. Kickelbick, N. Huesing, *J. Am. Chem. Soc.* **2001,** *123*, 9445-9446; b) X. Ye, C. Zhu, P. Ercius, S. N. Raja, B. He, M. R. Jones, M. R. Hauwiller, Y. Liu, T. Xu, A. P. Alivisatos, *Nat. Commun.* **2015,** *6*, 10052; c) G. A. Williams, R. Ishige, O. R. Cromwell, J. Chung, A. Takahara, Z. Guan, *Adv. Mater.* **2015,** *27*, 3934-3941

[13] a) V. B. Leffler, L. Mayr, P. Paciok, H. Du, R. E. Dunin-Borkowski, M. Dulle, S. Förster, *Angew. Chem. Int. Ed.* **2019,** *131*, 8629-8633; b) H. N. Kim, S. Yang, *Adv. Funct. Mater.* **2020,** *30*, 1902597; c) H. Tao, E. Galati, E. Kumacheva, *Macromolecules* **2018**, *51*, 6021-6027; d) C. Koh, G. S. Grest, S. K. Kumar, *ACS Nano* **2020,** *14*, 13491-13499; e) M. Xu, K. H. Ku, Y. J. Lee, T. Kim, J. J. Shin, E. J. Kim, S.-H. Choi, H. Yun, B. J. Kim, *Macromolecules* **2021**, *54*, 3084-3092.

[14] a) L. Cheng, A. Liu, S. Peng, H. Duan, *ACS Nano* **2010**, *4*, 6098-6104; b) J. Zhu, M. C. Hersam, *Adv. Mater.* **2017,** *29*, 1603895; c) J. Pang, S. Xiong, F. Jaeckel, Z. Sun, D. Dunphy, C. J. Brinker, *J. Am. Chem. Soc.* **2008,** *130*, 3284-3285; d) K. Ohno, K. Koh, Y. Tsujii, T. Fukuda, *Angew. Chem. In. Ed.* **2003,** *42*, 2751-2754; e) A. Dong, J. Chen, S. J. Oh, W.-k. Koh, F. Xiu, X. Ye, D.-K. Ko, K. L. Wang, C. R. Kagan, C. B. Murray, *Nano Lett.* **2011,** *11*, 841-846; f) H.-N. Barad, H. Kwon, M. Alarcón-Correa, P. Fischer, *ACS Nano* **2021**, *15*, 5861-5875.

[15] a) S.-K. Eah, *J. Mater. Chem.* **2011,** *21*, 16866-16868; b) S. Xiong, D. R. Dunphy, D. C. Wilkinson, Z. Jiang, J. Strzalka, J. Wang, Y. Su, J. J. de Pablo, C. J. Brinker, *Nano Lett.* **2013,** *13*, 1041-1046; c) T. P. Bigioni, X.-M. Lin, T. T. Nguyen, E. I. Corwin, T. A. Witten, H. M. Jaeger, *Nat. Mater.* **2006,** *5*, 265-270; d) T. Wen, S. A. Majetich, *ACS Nano* **2011**, *5*, 8868-8876; e) L. Song, B. B. Xu, Q. Cheng, X. Wang, X. Luo, X. Chen, T. Chen, Y. Huang, *Sci. Adv.* **2021,** *7*, eabk2852.

[16] a) H. Yun, J. W. Yu, Y. J. Lee, J.-S. Kim, C. H. Park, C. Nam, J. Han, T.-Y. Heo, S.-H. Choi, D. C. Lee, *Chem. Mater.* **2019**, *31*, 5264-5273; b) H. Yun, Y. J. Lee, M. Xu, D. C. Lee, G. E. Stein, B. J. Kim, *ACS Nano* **2020**, *14*, 9644-9651; c) I. Kosif, K. Kratz, S. S. You, M. K. Bera, K. Kim, B. Leahy, T. Emrick, K. Y. C. Lee, B. Lin, *ACS Nano* **2017**, *11*, 1292-1300; d) Y. H. Lee, W. Shi, H. K. Lee, R. Jiang, I. Y. Phang, Y. Cui, L. Isa, Y. Yang, J. Wang, S. Li, *Nat.Commun.* **2015,** *6*, 6990.

[17] Y. Wang, J. Chen, C. Zhu, B. Zhu, S. Jeong, Y. Yi, Y. Liu, J. Fiadorwu, P. He, X. Ye, *Nano Lett.* **2021,** *21*, 5053-5059.

[18] T. Kister, D. Monego, P. Mulvaney, A. Widmer-Cooper, T. Kraus, *ACS Nano* **2018**, *12*, 5969-5977.

[19] a) A. Dong, J. Chen, P. M. Vora, J. M. Kikkawa, C. B. Murray, *Nature* **2010**, *466*, 474-477; b) M. J. Campolongo, S. J. Tan, D.-M. Smilgies, M. Zhao, Y. Chen, I. Xhangolli, W. Cheng, D. Luo, *ACS Nano* **2011**, *5*, 7978-7985; c) A. Dong, X. Ye, J. Chen, C. B. Murray, *Nano Lett.* **2011,** *11*, 1804-1809.

[20] a) X. Lin, H. Jaeger, C. Sorensen, K. Klabunde, *J. Phy. Chem. B* **2001,** *105*, 3353-3357; b) S. Narayanan, J. Wang, X.-M. Lin, *Phy. Rev. Lett.* **2004,** *93*, 135503; c) N. Fleck, R. M. McMeeking, T. Kraus, *Langmuir* **2015**, *31*, 13655-13663; d) T. Kraus, L. Malaquin, E. Delamarche, H. Schmid, N. D. Spencer, H. Wolf, *Adv. Mater.* **2005,** *17*, 2438-2442; e) T. Kraus, L. Malaquin, H. Schmid, W. Riess, N. D. Spencer, H. Wolf, *Nat. Nanotechnol.* **2007,** *2*, 570-576; f) L. Qian, S. Zhai, Y. Jiang, B. Das, *J. Mater. Chem.* **2012,** *22*. 4932-4937; g) L. Malaquin, T. Kraus, H. Schmid, E. Delamarche, H. Wolf, *Langmuir* **2007**, *23*, 11513-11521; h) Y. Huang, W. Li, M. Qin, H. Zhou, X. Zhang, F. Li, Y. Song, *Small* **2017**, *13*, 1503339; i) Q. Yang, M. Deng, H. Li, M. Li, C. Zhang, W. Shen, Y. Li, D. Guo, Y. Song, *Nanoscale* **2015**, *7*, 421-425; j) M. Kuang, L. Wang, Y. Song, *Adv. Mater.* **2014,** *26*, 6950-6958; k) R. Buchheit, B. Kuttich, L. González-García, T. Kraus, *Adv. Mater.* **2021,** *33*, 2103087.

[21] a) S. Willing, H. Lehmann, M. Volkmann, C. Klinke, *Sci. Adv.* **2017,** *3*, e1603191; b) S. Srivastava, D. Nykypanchuk, M. Fukuto, O. Gang, *ACS Nano* **2014**, *8*, 9857-9866; c) D. Han, Y. Khan, J. Ting, S. M. King, N. Yaacobi-Gross, M. J. Humphries, C. J. Newsome, A. C. Arias, *Adv. Mater.* **2017,** *29*, 1606206; d) R. Janneck, F. Vercesi, P. Heremans, J. Genoe, C. Rolin, *Adv.Mater.* **2016,** *28*, 8007-8013.

[22] R. D. Deegan, O. Bakajin, T. F. Dupont, G. Huber, S. R. Nagel, T. A. Witten, *Nature* **1997**, *389*, 827-829.

[23] H. S. Kim, C. H. Lee, P. Sudeep, T. Emrick, A. J. Crosby, *Adv. Mater.* **2010**, *22*, 4600-4604.

[24] a) S. Ye, H. Zha, Y. Xia, W. Dong, F. Yang, C. Yi, J. Tao, X. Shen, D. Yang, Z. Nie, *ACS Nano* **2022**, *16*, 4609-4618; b) J. Che, K. Park, C. A. Grabowski, A. Jawaid, J. Kelley, H. Koerner, R. A. Vaia, *Macromolecules* **2016**, *49*, 1834-1847.

[25] a) K. J. Baeg, Y. Y. Noh, J. Ghim, B. Lim, D. Y. Kim, *Adv. Funct. Mater.* **2008,** *18*, 3678-3685; b) X. Gao, C.-H. Liu, X.-J. She, Q.-L. Li, J. Liu, S.-D. Wang, *Org. Electron.* **2014,** *15*, 2486-2491; c) Y. Kimura, A. Hamaguchi, Y. Ikeda, T. Nagase, H. Naito, K. Takimiya, T. Shiro, *Appl. Phys. Express* **2015,** *8,* 101601; d) C.-C. Shih, Y.-C. Chiang, H.-C. Hsieh, Y.-C. Lin, W.-C. Chen, *ACS Appl. Mater. Interfaces* **2019,** *11*, 42429-42437.

[26] D. Doblas, T. Kister, M. Cano-Bonilla, L. González-García, T. Kraus, *Nano Lett.* **2019,** *19*, 5246-5252.

[27] T. Kister, J. H. Maurer, L. González-García, T. Kraus, *ACS Appl. Mater. Interfaces* **2018,** *10*, 6079-6083.

[28] A. Oron, S. H. Davis, S. G. Bankoff, *Rev. Mod. Phys* **1997,** *69*, 931-980.

[29] a) A. Yarin, J. Szczech, C. Megaridis, J. Zhang, D. Gamota, *J. Colloid Interface Sci.* **2006,** *294*, 343-354; b) F. G. Schofield, A. W. Wray, D. Pritchard, S. K. Wilson, *J. Eng. Math.* **2020,** *120*, 89-110.

Entry for the Table of Contents

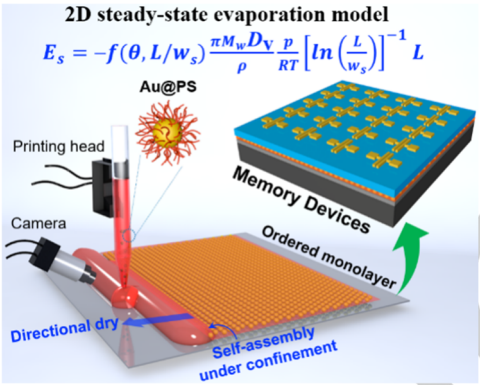

A printing approach is developed to address the challenge of in situ fabrication of macroscale ordered self-assembled monolayers of nanoparticles at targeted locations on substrates. A 2D diffusion-controlled steady-state evaporation model is proposed to explain the mechanism. The ordered monolayer exhibits good performance for nonvolatile nanocrystal floating gate memory devices.